



Strength through curvature: Engineering multi-phase materials based on chiral aperiodic monotile patterns

Jiyoung Jung¹, Kundo Park¹, Grace X. Gu^{*}

Department of Mechanical Engineering, University of California, Berkeley, CA 94720, USA

ARTICLE INFO

Keywords:

Chiral aperiodic monotile
Fracture resistance
Bayesian optimization
Additive manufacturing
Phase-field models

ABSTRACT

Developing new materials with superior mechanical properties is crucial in various engineering applications. This study introduces novel multi-phase materials created using chiral aperiodic monotile patterns, distinguished by their curved edges and ability to cover a surface without translational symmetry. We employ multi-objective Bayesian optimization and crack phase-field modeling to explore the mechanical properties of the chiral aperiodic monotile composites, considering the topology, volume fraction, and constituent materials as design variables. Pareto-optimal designs are selected for experimental validation using additive manufacturing and mechanical testing. The experimental results show that these aperiodic composites exhibit an improved balance of mechanical properties, including strength, work of fracture, and failure strain, that typically involve trade-offs in conventional periodic structures. This is primarily attributed to the superior interlocking effect introduced by the curved edges, leveraging the load-bearing capacity of both constituent materials. Additionally, our findings show that the toughening mechanisms and crack propagation paths of these aperiodic composites can be tuned to undergo different failure modes from brittle to ductile fracture along the Pareto front, highlighting the composite's exceptional ability to be tailored for different design purposes. This research underscores the potential of chiral aperiodic monotiles, paving the way for developing high-performance structural materials.

1. Introduction

Tiling patterns are prevalent in diverse contexts, ranging from artistic designs to mathematical arrangements to natural formations. Recent discoveries of tiling patterns have inspired novel designs for structural materials [1–5]. For instance, the complex fractal geometries and hierarchical structures found in nature have been used to create various composite materials that exhibit excellent mechanical performance across multiple scales [6–11]. The quasicrystals, with their ordered but non-periodic arrangement of atoms, have allowed the material to exhibit uncommon properties, such as low thermal conductivity and reduced surface friction [12–14]. Also, the quasiperiodic material structures based on the Penrose pattern have enabled increased microwave absorption [15,16]. Overall, theories and discoveries in the field of tiling patterns serve as a significant source of inspiration for the next generation of advanced materials.

A noteworthy development in the field of mathematical tiling is the discovery of the aperiodic monotile, with the 'hat' being the first of its kind to be found [17]. An aperiodic monotile is a single tile shape that

can fill a two-dimensional plane without a periodic pattern, meaning it does not exhibit translational symmetry. The advent of aperiodic monotile holds significant promise for materials engineering, due to its ability to achieve nearly isotropic mechanical properties while maintaining high assembly efficiency due to the use of a single shape. Several studies have focused on aperiodic monotile-based lattice structures. Recent research has shown that metamaterials with a near-zero Poisson's ratio based on the 'hat' aperiodic monotile can be created [18]. The study has revealed that the aperiodicity within the structure allows the material to maintain an extremely low Poisson's ratio almost uniformly in all directions. While exploring the elastic behavior such as elastic moduli and auxeticity of metamaterials is crucial [19,20], it is also important to investigate their failure mechanisms beyond the elastic regime. Researchers have designed a metamaterial featuring microlattices with aperiodic unit cells that exhibit high strength, tensile toughness, and damage tolerance under external compression [21]. Their analysis has highlighted that the enhancement in performance against compressive loads is due to the aperiodicity, which creates diverse local failure thresholds as a result of varying strut angles and

* Corresponding author.

E-mail address: ggu@berkeley.edu (G.X. Gu).

¹ These authors contributed equally to this work.

contact modes during compression. Recently, we have utilized the ‘hat’ aperiodic monotile pattern to create a two-phase composite material [22], demonstrating that composites based on aperiodic monotile exhibit superior Young’s modulus, strength, and work of fracture compared to composites with periodic patterns under tensile loading. Additionally, the aperiodic monotile structures maintain consistent mechanical performance despite variations in locations and directions of a notch, indicating reliable fracture resistance under complex loading conditions. These studies have primarily investigated the characteristics of ‘hat’ aperiodic monotile structures, highlighting nearly isotropic properties and their superior mechanical performance compared to conventional periodic structures. However, the exploration has been limited to a design space where the edges of the monotile are composed of straight lines, leaving opportunities to discover designs that can further enhance the performance of the composites. Meanwhile, the strictly chiral aperiodic monotile, also referred to as ‘Spectres’, is a unique class of aperiodic monotiles discovered later where the straight edges are replaced with asymmetrical curves [23].

In this study, we introduce a chiral aperiodic monotile patterned structure aimed at enhancing the fracture resistance of composites. Like conventional aperiodic monotile structures with straight edges, chiral aperiodic monotile structures leverage the structural advantages of aperiodicity and the design simplicity of tiling an infinite plane with a single type of tile, which is an attribute absent in conventional periodic designs. Additionally, the introduction of curved edges expands the design space of aperiodic monotile structures, potentially allowing for fine-tuning of mechanical performance. Furthermore, these curved edges are expected to enhance the interlocking effect between tiles, thereby maximizing the load-bearing capacity of the reinforcements. To identify the optimal chiral aperiodic monotile pattern designs that achieve an excellent balance of key mechanical properties, including strength, work of fracture, and ductility, we employ a machine-learning-based optimization framework. The design parameters include the curvature amplitude of the monotile edges, the relative volume fraction of the two constituent materials, and the type of materials used for the composite. Employing multi-objective Bayesian optimization (MBO) [24,25] coupled with crack phase-field simulation, we explore the optimal input values to design high fracture resistance composites. MBO can efficiently identify the Pareto front of multiple objectives in trade-off relationships [26]. The phase-field modeling is utilized to examine the mechanical properties of the chiral aperiodic monotile composites where the model can simulate complex crack evolution phenomena, such as curvilinear crack paths and crack branching [27–30]. The optimal designs generated by the simulation data-based MBO are validated by fabricating them with 3D printers and conducting uniaxial tensile tests. It is envisioned that this study to explore the optimal design of chiral aperiodic monotile composite using machine-learning-based optimization opens a new era of advanced structural materials with superior fracture resistance, enhanced durability, and tailored mechanical properties that can be precisely engineered for specific applications.

2. Results and discussion

This section presents the optimization results obtained through MBO and the experimental validation for chiral aperiodic monotile-based composites. Section 2.1 introduces the fundamental characteristics of aperiodic monotile structures and provides initial findings on their fracture behavior. Section 2.2 defines the optimization problem by detailing the input parameters and objectives. Section 2.3 presents the optimization results obtained through MBO integrated with the crack phase-field model to identify high-performance designs. Finally, Section 2.4 experimentally validates the optimized designs, verifying their performance and mechanical properties.

2.1. Exploring the mechanical behavior of chiral aperiodic monotile-based composites

Among the various aperiodic monotiles, the ‘equilateral polygon’ monotile has an identical length between each point as shown in the left top of Fig. 1a. Chiral aperiodic monotile, so-called ‘Spectres’, is formed by modifying the edges of aperiodic monotile into curves as shown in Fig. 1a. Fig. 1b shows how the chiral aperiodic monotile structure varies depending on the curvature of edges. In this study, the change in curvature is defined by the amplitude of the spline curves. Further information on the generation of chiral aperiodic monotile composite patterns is provided in the **Experimental Section**.

In our previous work, we have investigated the fracture behavior of a ‘hat’ aperiodic monotile composite structure, which consisted of digital photopolymer materials: VeroClear (stiff cores) and TangoBlackPlus (soft boundaries) [22]. The study demonstrates that the aperiodic monotile-based composite exhibited superior fracture resistance compared to the other periodic structures due to the complex crack path of the aperiodic monotile. We notice, however, that the cracks only propagate along the boundaries of the aperiodic monotiles. The reason for this is due to the limited volume fractions of cores (70 %–80 %), predetermined material combinations, and straight boundaries. This indicates that the load-bearing capacity of stiff cores may not be fully utilized, implying that the fracture performance or resilience can be further enhanced by developing an architecture and material composition that efficiently utilizes the load-bearing capacity of both phases. In this respect, we believe that the chiral aperiodic monotile structure, with curved edges, has the potential to better leverage the load-bearing capacity of cores by continuously inducing more crack deflections and stronger interlocking of monotiles. Additionally, using thinner boundaries and selecting stiffer boundary materials can also increase the load-bearing capacity of the cores.

As an initial study, structural effects with varying curve amplitudes and volume fractions are investigated in Fig. 2. VeroClear (cores) and TangoBlackPlus-based (boundary) photopolymer materials are chosen since these two types of materials demonstrate excellent interfacial bonding [31]. The crack paths of specimens with varying curvature amplitudes are presented in Fig. 2a, which demonstrates that the failure mode of the chiral aperiodic monotile composite can be varied by the curvature of the monotile. Here, the amplitude of curvatures is varied as $A = [0.00 \text{ mm}, 0.50 \text{ mm}, 0.75 \text{ mm}]$ while the volume fraction ($\rho = 80.0 \%$) and types of material (FLX9050 for boundary and Veroclear for cores) are fixed. Higher curvature leads to straight crack propagation through the cores, potentially increasing the ultimate strength but reducing the work of fracture and ductility due to brittle fracture. In contrast, patterns with straight edges cause zigzag crack propagation along the boundary phase, potentially resulting in higher ductility but lower strength. An intermediate curvature produces a mix of failure modes, accompanying both highly deflected crack path and monotile fracture. The crack paths of specimens with respect to different volume fractions are presented in Fig. 2b. Again, Veroclear and FLX9050 are used for cores and boundaries, respectively. The results show that the specimen with a lower volume fraction of cores allows cracks to propagate along the soft boundaries, which is a failure mode that promotes higher ductility. The specimen with a higher core volume fraction causes cracks to penetrate the stiff cores, a failure mode that leads to higher strength yet higher brittleness. With an intermediate volume fraction, both zigzag and straight crack propagation modes occur, which can potentially result in a well-balanced combination of strength and ductility in the mechanical properties. In summary, high curvature of the patterns, a high core volume fraction, and a stiff boundary material tend to induce crack penetration through the cores; whereas low curvature of the patterns, a low core volume fraction, and a soft boundary material promote crack propagation along the boundary. Since crack behavior is determined by the interaction of these three design parameters, even in a chiral aperiodic monotile composite design with high

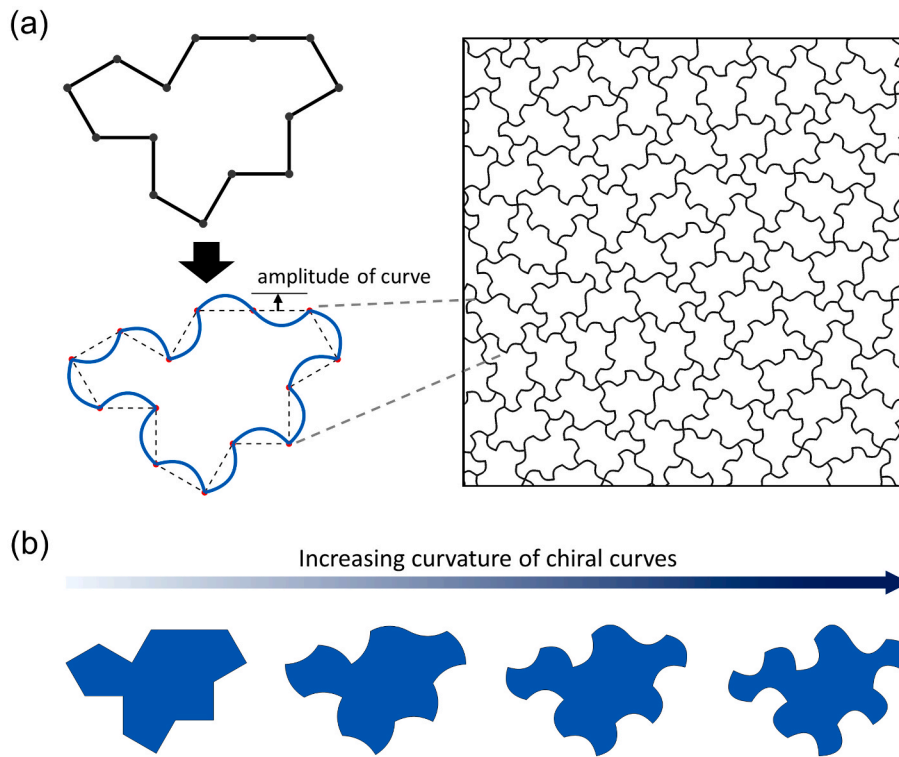


Fig. 1. (a) Schematic representation of ‘equilateral polygon’ monotile (top left), ‘Spectre’ chiral aperiodic monotile (bottom left), and its tiling image. (b) Variations in the shape of chiral aperiodic monotile according to the curvature of the curves.

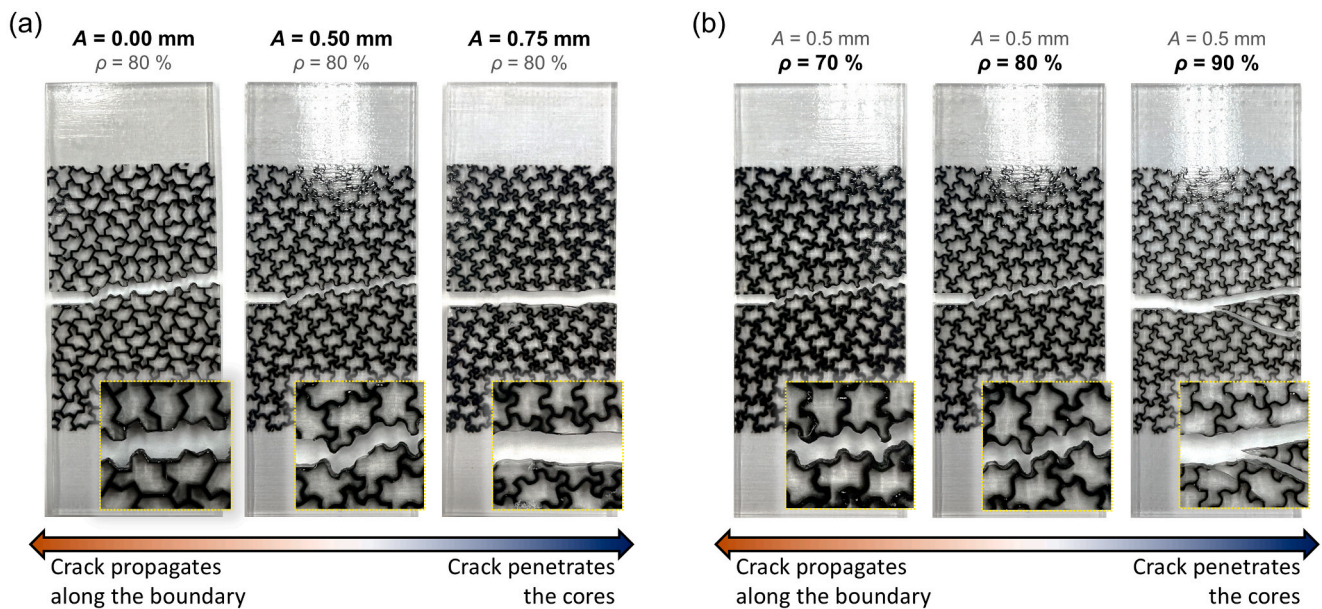


Fig. 2. Different failure morphologies observed depending on (a) the curvature of chiral aperiodic monotile and (b) the volume fraction of composites: crack propagation mechanisms penetrating the cores and detouring along the boundary.

curvature, if the core volume fraction is low and the boundary material is soft, the crack may propagate along the boundary. From this initial analysis, we find that chiral aperiodic monotile-based composites can have a diverse range of failure behaviors, which enables tunable designs for chiral aperiodic monotile composites. This capability can be beneficial for structural applications where ductile, brittle, or balanced fracture modes are required. As such, we seek to systematically explore their mechanical properties by employing an optimization framework

with varying geometry, composition, and material combinations.

2.2. Formulation of the optimization problem

To optimize the chiral aperiodic monotile composites, an optimization problem is defined with three independent design variables [volume fraction of hard material (ρ), the amplitude of the curve (A), and type of soft material (m)], and three objective functions [ultimate

strength, work of fracture, and failure strain]. In this study, the work of fracture is defined as the total fracture work divided by the initial ligament area of the notched sample during its failure process, calculated as the area under the stress-displacement curve. Failure strain is chosen as a quantitative measure of ductility, recognizing that it is one of several indicators used to assess the material's deformation capacity. As discussed earlier, these three design variables are important design parameters of chiral aperiodic monotile composites that significantly affect the failure morphology and, thus, the three objective functions. Consequently, identifying their optimal values is critical for building a chiral aperiodic monotile composite with an excellent balance of strength, work of fracture, and failure strain. The ranges of the three design variables are set as follows,

$$\rho \in [70.0\%, 72.5\%, 75.0\%, 77.5\%, 80.0\%, 82.5\%, 85.0\%, 87.5\%, 90.0\%],$$

$$A \in [0.000\text{mm}, 0.250\text{mm}, 0.375\text{mm}, 0.500\text{mm}, 0.625\text{mm}, 0.750\text{mm}],$$

$$m \in [\text{FLX980}, \text{FLX9040-DM}, \text{FLX9050-DM}, \text{FLX9060-DM}, \text{FLX9070-DM}, \text{FLX9085-DM}, \text{FLX9095-DM}]$$

Non-continuous design variables having discrete levels are considered in this study for the following reasons. First, we consider ρ and A as discrete variables to balance computational efficiency and design freedom. For the material variable m , the choices are constrained to those offered by the PolyJet printer, specifically mixtures of TangoBlackPlus (primary material) and VeroClear (secondary material) in varying compositions. We choose VeroClear for the stiff core section without varying the material type for this section, as minimal differences are observed in the mechanical properties across VeroClear-dominant material selections (RGD810, RGD8705, RGD8710, RGD8615, RGD8720, RGD8725, and RGD8625). Given that the discretization of input parameters is sufficiently fine and uniform, the resulting optimization results can approximate that of a continuous design space.

In this research, a crack phase-field model implemented in the ABAQUS User subroutine is adopted to compute the three objective functions: ultimate strength, work of fracture, and failure strain for chiral aperiodic monotile composites under uniaxial tension. The crack phase-field algorithm is capable of modeling various composite failure phenomena, such as crack nucleation, crack branching, and crack coalescence, without having to provide a predefined crack path, which is an advantage over other fracture modelings (e.g. cohesive element model [32]). Recent advances in the crack phase-field algorithm have enabled

the simulation of not only brittle fracture but also various other fracture types, including anisotropy, elastoplasticity, viscoelasticity, and even fatigue failures [33,34]. The model's high degree of customizability further allows researchers to implement specific failure mechanisms tailored to their studies or to incorporate multiphysical phenomena such as temperature variations or changes in electrical resistance during material deformation and failure [35,36].

In the simulation, a two-dimensional specimen has dimensions of 75 mm by 50 mm as shown in Fig. 3a. A single-edge notch with a length of 10.0 mm (20 % width of the specimen) and a thickness of 0.5 mm is introduced in the specimen, and the notch tip is located on the soft phase. In this study, we consider notched specimens to observe and capture the crack propagation behavior of the designed composites. Additionally, placing a notch in the sample prevents crack formation and propagation near the grip section, ensuring it propagates within the desired section of the composite. The material properties for the phase-field model are fitted through a tensile test of a single-phase specimen. The fitted Young's moduli (E) and critical energy release rates (g_c) for each phase are presented in Table S1 (See Section 1 of the Supporting Information). Further information on the phase-field model, experimental setup, and material property fitting is provided in the Experimental Section. In this study, the simulation results are considered as ground truth for our data-driven approach discussed next.

2.3. Determination of high-performance designs via multi-objective Bayesian optimization

Bayesian optimization is employed to efficiently explore the design space defined above. Bayesian optimization is a data-driven strategy to sequentially explore a design space, aiming to identify the global optimum in a data-efficient way, especially when the objective function is expensive to evaluate and the design space is reasonably small. Under these circumstances, MBO is renowned for significantly outperforming other data-driven optimization algorithms (such as NSGA) by generating a more diverse set of Pareto-optimal solutions within limited design generations [37]. This is due to the excellent balance of exploitation (focusing on the regions near the current best solution) and exploration (exploring uncharted regions in the design space) of MBO, resulting in a broader range of optimal design solutions. MBO offers a versatile framework that has been applied across a wide range of engineering designs including material structure, chemical components, and even manufacturing processes [38–41]. Moreover, active research is

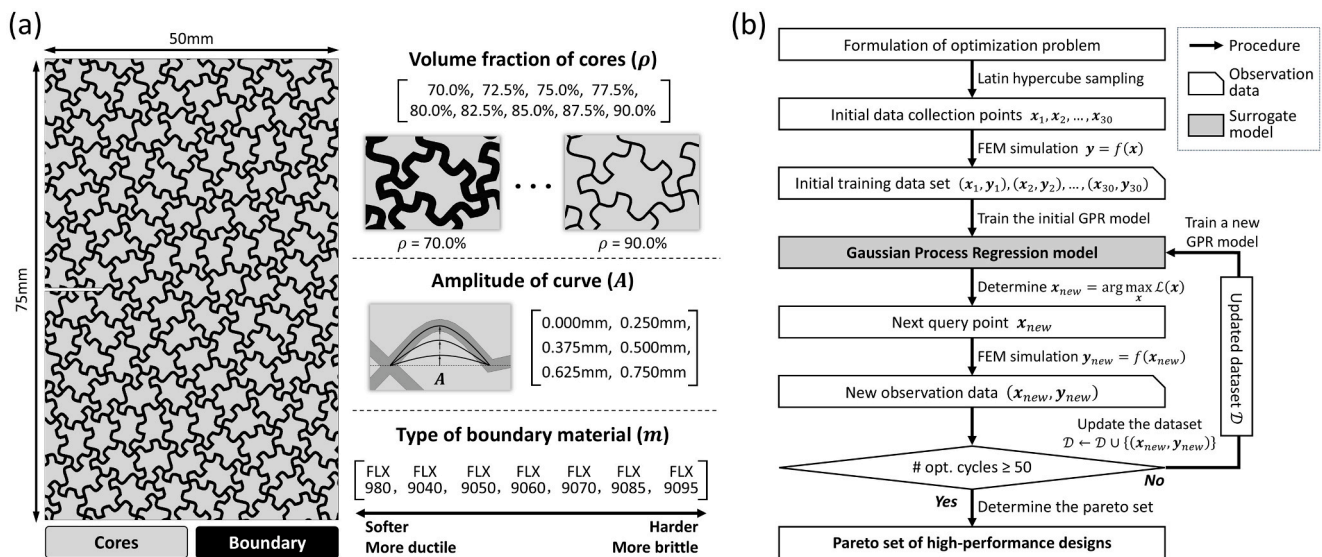


Fig. 3. Formation of chiral aperiodic monotile composite design problem. (a) Graphical representation of the design variables. (b) Overall workflow chart of the multi-objective Bayesian optimization (MBO) framework employed in this study.

underway to further enhance MBO for specialized applications such as physics-based MBO [42]. Fig. 3b illustrates the optimization process in a schematic flowchart. In this research, we use Gaussian process regression (GPR) as a surrogate model, which is the most commonly used regression model for Bayesian optimization. To prepare the initial training dataset for our initial GPR model, 30 distinct input

combinations are chosen within the three-dimensional design space using the Latin hypercube sampling method. Then, the objective function values of the 30 different input combinations are computed with crack phase-field simulation, and the result is presented in Fig. 4.

Using the initial training data set, we train our initial GPR model. An important matter to consider in this study is that the design variables are

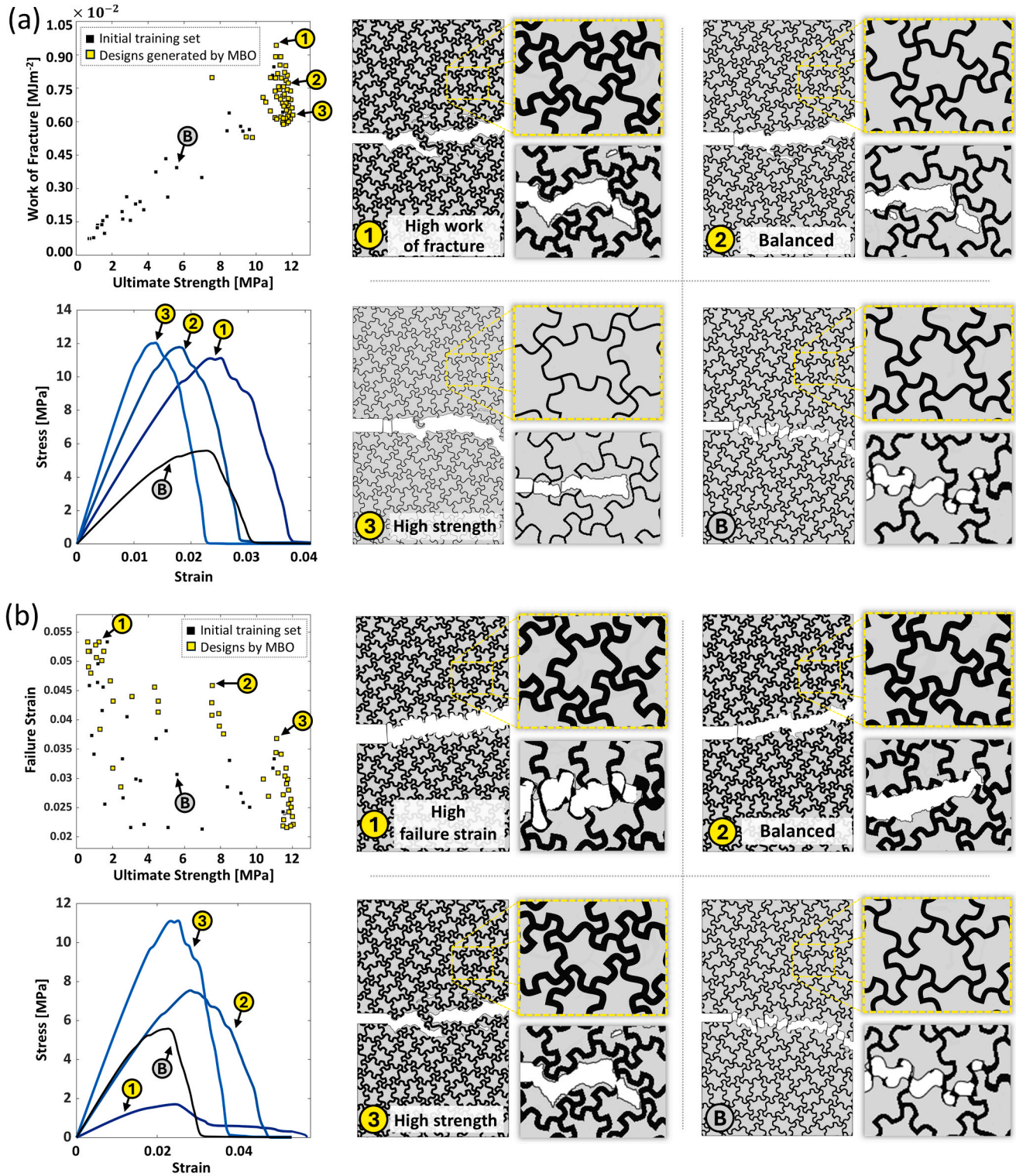


Fig. 4. Results of optimization process. MBO is performed for two distinct design criteria: (a) High strength-work of fracture design and (b) High strength-failure strain design. The scatter plot visualizes the 30 initial training data and 50 MBO-generated data on the objective function space. Three representative designs are selected from the Pareto-optimal design solutions, and their mechanical performance is compared against a baseline design from the initial training set.

'non-continuous' as each design variable consists of discrete levels of candidates. To effectively handle our discrete design space, we implement a special GPR model recently developed by Garrido-Merchan et al, which is capable of modeling both continuous and discrete variable types [43]. The trained surrogate model allows for the probabilistic prediction of objective function values at unknown design points. Using the trained GPR, Bayesian optimization repeatedly samples a new data point at the location maximizing the value of the acquisition function. Here, Expected Hypervolume Improvement (EHVI) is adopted as our acquisition function to consider both exploration and exploitation in a balanced manner to choose the next query point [44]. The EHVI function aggregates multiple objectives and may be dominated by the objective function that has a bigger value range. To ensure that objective functions contribute more equitably, we use the min–max scaling method to normalize the objective function values, so that all three objective functions can vary between 0 and 1 (strength: [0, 12] MPa, work of fracture: [0, 0.009]MJm⁻², failure strain: [0.019, 0.06]). A detailed explanation of the implementation of MBO can be found in the **Experimental Section**.

Starting with the GPR model trained with 30 initial training data, we performed 50 repetitions of MBO sampling in order to determine the Pareto-optimal sets of design variable values that allow us to produce chiral aperiodic monotile composites having a good balance of strength, work of fracture, and failure strain. In this research, we conduct MBO on two distinct cases: one focused on designing a high strength and work of fracture composite, and the other aimed at creating a high strength and failure strain composite.

Fig. 4 presents the result of MBO and the failure mode of several highly performing designs proposed by MBO, where Fig. 4a is about the optimization for high strength-work of fracture, and Fig. 4b is about the optimization for high strength-failure strain. In the scatter plot located in the upper-left corner of each figure, the ultimate strength, work of fracture, and failure strain of the 30 initial designs are depicted with black square markers. The progression over 50 iterations of MBO is represented by yellow square markers. The scatter plots show that our MBO-based composite designing framework can generate high-performance composite designs that have an optimal balance of multiple mechanical properties, representing the Pareto-optimal solutions. Comparing the scatter plots in each figure reveals that strength and work of fracture generally exhibit a positive correlation, leading to a narrow data distribution along the diagonal with a relatively small number of Pareto-optimal designs. Conversely, strength and failure strain display a strong trade-off relationship, resulting in an extensive Pareto front and a variety of Pareto-optimal designs.

From all the Pareto-optimal design solutions determined with MBO, we select three representative designs and analyzed their failure process to understand the mechanisms behind their exceptional mechanical properties. The three designs optimized for strength and work of fracture (shown as yellow circled numbers in Fig. 4a) commonly have a high curve amplitude ($A = 0.75$ mm) and a high-strength boundary material ($m = \text{FLX9095-DM}$). Regarding design variable A , the result indicates that an aperiodic monotile pattern with highly curved edges enhances the interlocking effect of stiff core materials, which is the primary load-bearing components. This enables the overall structure to withstand higher external loads, thereby improving both strength and work of fracture. Regarding design variable m , the strongest material candidate for the boundary, despite its low ductility, is preferred because it facilitates more load transfer to the stiff reinforcements. If a softer material is chosen, cracks would propagate primarily through the soft boundary, failing to effectively utilize the load-bearing capacity of the stiff reinforcements. The balance between strength and work of fracture can be controlled by changing the relative volume content parameter ρ , which is closely related to the thickness of boundary material in the composite. Having a thicker boundary allows the structure to focus better on the work of fracture (the total energy absorbed by the material) by forcing the crack to propagate in a zigzag pattern, thereby absorbing more

energy during the failure process (Design 1). On the other hand, reducing the thickness of the boundary allows the structure to focus better on its strength by forcing the crack to propagate straight through the stiff core materials (Design 3). Compared to a baseline design randomly selected from the initial training data, it can be noted from the stress–strain curves that the Pareto-optimal solutions exhibit significantly improved mechanical properties: the strength and work of fracture of the optimal Design 2 is 105 % and 98 % higher than that of the baseline design, respectively.

The three designs optimized for strength and failure strain (shown as yellow circled numbers in Fig. 4b) commonly have a high amplitude of curve ($A = 0.75$ mm) and low volume content of core materials ($\rho = 70$ %). Regarding the design variable A , the high amplitude of the curve leads to a stronger interlocking effect between the monotiles, improving the strength of the composite design. A high amplitude curve also benefits failure strain, as it guides the crack to propagate along a more curved path before the material reaches complete failure. In terms of design variable ρ , a thicker boundary layer is preferable for designing strong and ductile composites. The soft boundary layer is the primary source of ductility for the composite, and reducing its thickness would significantly increase brittleness, offering only minimal improvement in ultimate strength. By adjusting the remaining design parameter m , the balance between the two objective functions can be customized. Selecting a stronger and more brittle material for the boundary region, such as FLX9095-DM, allows us to focus more on ultimate strength (Design 3), while choosing a softer and more ductile material, like FLX9040-DM, prioritizes improving failure strain (Design 1). By choosing an intermediate material, such as FLX9085-DM, we could design a chiral aperiodic monotile composite that has balanced strength and failure strain (Design 2). Compared to a baseline design randomly selected from the initial training data, it can be noted from the stress–strain curves that the Pareto-optimal solutions had significantly improved mechanical properties (the strength and failure strain of the optimal Design 2 being 35 % and 48 % higher than that of baseline design, respectively). These results highlight the potential of chiral aperiodic composite to control how the cracks propagate in heterogeneous material and, if optimally designed for efficient load bearing, to result in exceptionally improved mechanical performance.

One interesting point to note from these two separate optimization cases is that some of the Pareto optimal solutions determined from the strength-work of the fracture case are also found in the Pareto sets from the strength-failure strain case (at the bottom right corner of the scatter plot). This is primarily because the work of fracture inherently represents the balance of strength and failure strain. While some Pareto optimal designs appear in both strength-work of fracture and strength-failure strain optimizations, the MBO algorithm generates significantly different data points depending on the chosen objective. In strength-failure strain optimization, the MBO explores a wide range of mechanical properties, searching for diverse Pareto optimal designs across the design space (encompassing both the highly ductile Design 1 and brittle design at to bottom right corner). Conversely, when optimizing for strength-work of fracture, the MBO focuses on a narrower region, prioritizing high strength-high work of fracture designs and ignoring excessively ductile designs that compromise strength. Therefore, strength-failure strain optimization can be favored for exploring a wide range of failure modes while strength-work of fracture optimization can be preferred for a data-efficient search for fracture resistance. The relationships between inputs and objectives are visualized as scatter plots in Section 2 of **Supporting Information**, providing their overall correlations.

2.4. Validation of the high-performance chiral aperiodic monotile composites through experiment

Experimental validation is conducted on the optimal chiral aperiodic monotile composite designs obtained in Section 2.3. To verify the

superiority of the optimal designs, the representative Pareto-optimal designs and the baseline design depicted in Fig. 4 (with and without curved edges) are printed using Polyjet additive manufacturing. In addition, we also consider periodically structured composites (featuring square and hexagonal lattice structures) as benchmark models and compare their mechanical performances to that of our optimized chiral aperiodic monotile composite designs. Here, the design variables for the benchmark models are selected through the process elaborated in Section 3 in the Supporting Information to ensure that we are comparing our designs to highly performing benchmarks. Three specimens are tested for each design to consider experimental deviation. In Fig. 5, the tensile test results for the optimized chiral aperiodic monotile composites (obtained from strength-work of fracture and strength-failure strain optimizations) are compared to those of the baseline designs and benchmarks. The failure morphologies of all tested specimens used in the validation study are presented in Section 4 of the Supporting Information.

Fig. 5a presents the results of strength-work of fracture optimization where the strength-based selected specimen shows the highest strength, the work of fracture-based selected specimen shows the highest work of fracture, and the balanced specimen shows the middle, matching with the obtained Pareto curve. It can be noted from the failure morphology of the specimens that the cracks are propagated through the stiff cores, as these designs are optimized to maximally leverage the stiff core material for high strength and work of fracture. Fig. 5b presents the results of strength-failure strain optimization. As predicted in the Pareto curve, the strength-based selected specimen shows the highest strength, the failure strain-based selected specimen shows the highest failure strain, and the balanced specimen shows the middle. The failure morphology of the specimens reveals that the strength-focused composite fails with a straight crack while the failure strain-focused composite exhibits crack

propagation through a highly deflected boundary phase, which is the main source of its ductility. In both optimization cases, the optimized designs commonly have a high amplitude of curves, which would increase the interlocking effect among tiles. The results of baseline designs from Fig. 4 are presented in grey lines for comparison where the ‘Chiral AP’ features curved edges, and the ‘Standard AP’ refers to an ‘equilateral polygon’ monotile with straight edges. In general, the designs optimized using MBO demonstrate significantly improved mechanical properties compared to the baseline aperiodic designs because the optimized designs enable the overall structure to more effectively utilize the load-bearing capacities of both the stiff core material and the ductile boundary material. Compared to the standard aperiodic monotile composite with straight edges, merely incorporating curved edges results in simultaneous improvements of 14.7 % in strength, 20.5 % in work of fracture, and 3.6 % in failure strain. Moreover, by applying multi-objective Bayesian optimization to fine-tune the design variables, we can determine multiple Pareto-optimal design solutions that have an optimal balance of multiple mechanical properties. Notably, the design optimized for balanced strength and failure strain achieves remarkable enhancements compared to the standard aperiodic monotile composite: 47.4 % in strength, 89.8 % in work of fracture, and 16.4 % in failure strain.

In Fig. 5c, the results for periodically structured composites (including square and hexagon patterns) are shown as benchmarks. Table 1 summarizes the strength, work of fracture, and failure strain values for both the optimized chiral aperiodic monotile designs and benchmark designs. Overall, the optimized chiral aperiodic monotile composites exhibit enhanced strength, work of fracture, and failure strain compared to the square and hexagon-tiled benchmark designs. Since optimized hexagon composites exhibit the best performance among benchmark designs, we consider the design as a primary

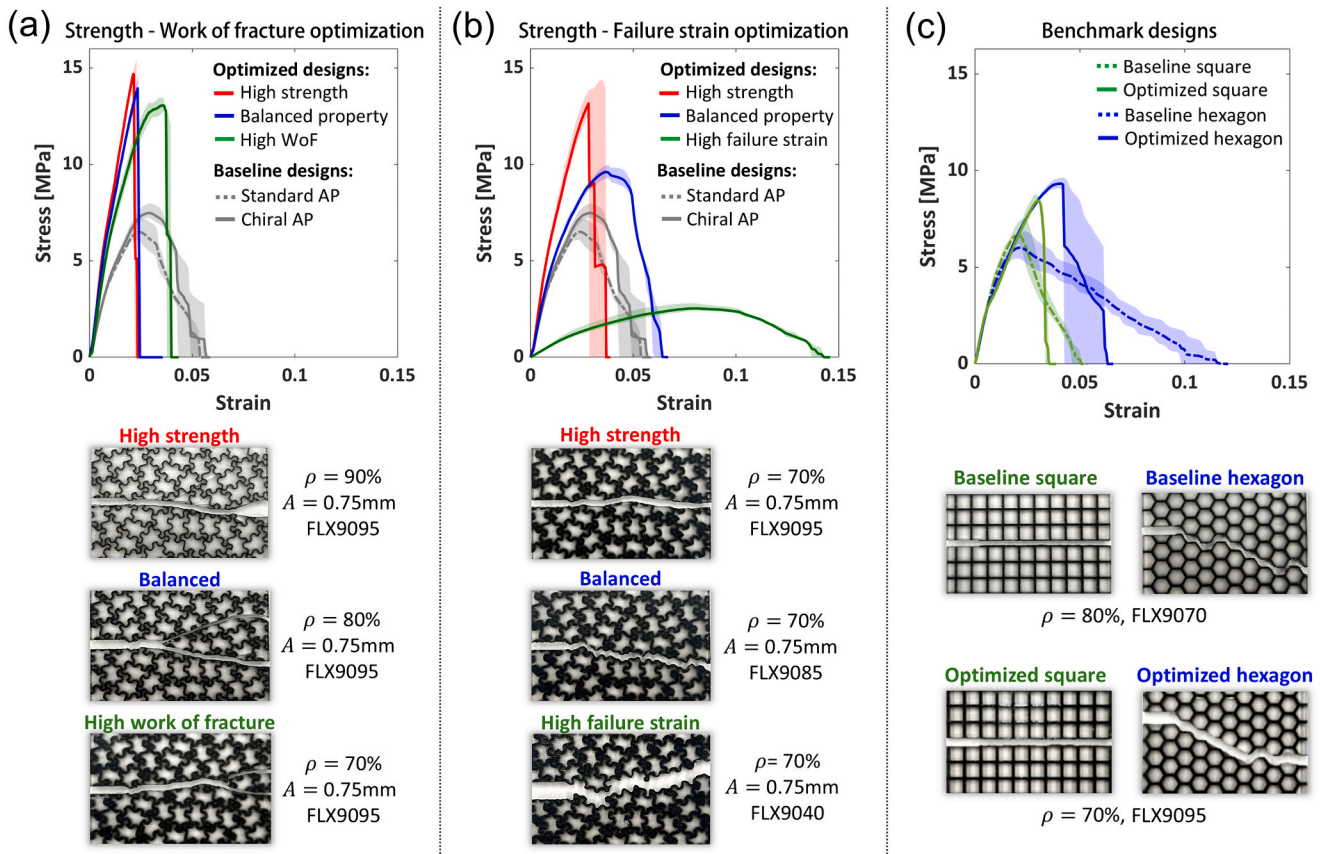


Fig. 5. Validation of the properties of chiral aperiodic monotile composites through experiments. Tensile test results of the chiral aperiodic monotile composites from (a) strength-work of fracture optimization and (b) strength-failure strain optimization. (c) Tensile test results for benchmark designs.

Table 1

Mechanical properties of optimized chiral aperiodic monotile composite specimens compared to that of benchmark specimens. The values presented are the mean of three tensile test trials repeated on each design.

	Design criteria	Strength [MPa]	Work of fracture [MJ/m ²]	Failure strain
Strength – Work of fracture optimization	High strength	14.69	0.0137	0.023
	Balanced strength-work of fracture	13.94	0.0142	0.025
	High work of fracture	13.06	0.0257	0.040
Strength – Failure strain optimization	High strength	13.16	0.0201	0.033
	Balanced strength-failure strain	9.61	0.0306	0.064
	High failure strain	2.53	0.0182	0.143
Baseline designs	Standard aperiodic monotile	6.52	0.0161	0.055
	Chiral aperiodic monotile	7.48	0.0194	0.057
Benchmark designs	Baseline square-tiled	5.74	0.0117	0.051
	Baseline hexagon-tiled	5.18	0.0230	0.116
	Optimized square-tiled	8.45	0.0133	0.036
	Optimized hexagon-tiled	9.33	0.0256	0.063

benchmark for quantitative comparison with chiral aperiodic monotile composites. Comparing the results of the strength-work of fracture optimization to the primary benchmark, the chiral aperiodic monotile composite optimized for strength shows a 57.5 % increase in strength, and even the composite optimized for work of fracture exhibits 40.0 % improvement in strength while retaining nearly the same level of work of fracture. The chiral aperiodic monotile composites optimized for strength-failure strain also exhibit an excellent balance of mechanical properties. The chiral aperiodic monotile composite optimized for strength shows a 41.1 % increase in strength, and the composite optimized for failure strain exhibits a 127.0 % improvement in failure strain, compared to the primary benchmark. To evaluate the improvement in the objective functions with a trade-off relationship, a product of the objectives is considered. In strength-work of fracture optimization, the chiral aperiodic monotile composite achieves up to 0.0454 MPa • MJm⁻² for the product of strength and work of fracture, demonstrating a 51.6 % improvement over the benchmark design. On the other hand, in strength-failure strain optimization, the chiral aperiodic monotile composite attains up to 0.198 MPa for the product of strength and failure strain, representing a 5.9 % improvement over the benchmark design. The above experimental validation reveals that optimized chiral aperiodic monotile composites exhibit enhanced mechanical performance as well as the ability to be tailored for their intended objectives compared to the periodic benchmark structures. The curved edges in the chiral aperiodic monotile pattern enable us to adjust the failure mode of the composite, offering a high degree of design flexibility in mechanical properties. Our framework demonstrates efficient exploration of the design space and identification of the optimal combination of design variables, resulting in a good balance of mechanical properties.

Based on the results of the two optimization cases, a higher curve amplitude is favored for the optimized chiral aperiodic monotile composites, which can be attributed to several key factors. First, a higher curve amplitude enhances the interlocking effect between stiff cores, improving overall structural integrity. Additionally, it introduces a wavy soft boundary, which promotes the formation of longer crack paths, leading to greater energy dissipation, crack deflection, and crack bridging. This design achieves a compromise between allowing cracks to penetrate the high-strength cores and encouraging crack propagation along the softer boundary, where the extended crack path increases energy dissipation. In this regard, the optimized chiral aperiodic monotile composites exhibit high strength when cracks predominantly penetrate the core tiles, while they demonstrate high failure strain when cracks primarily propagate along the boundaries. By carefully balancing strength, fracture energy, and failure strain, which inherently involve trade-offs, balanced mechanical performance can be achieved by an optimal combination of core penetration and boundary propagation. In addition to the excellent tunability, the random nature of the aperiodic monotile pattern allows the overall composite to have nearly isotropic material properties in all directions, which is an important feature in

real-life structural applications where external loads may be applied in various directions. These results underscore the broad practical applicability of chiral aperiodic composites as structural materials in various fields where tailored fracture characteristics are required, such as aerospace, automotive, protective gear, and biomedical industries.

3. Conclusions

This study performs design optimization of chiral composite using MBO, exploring a wide range of mechanical properties. The chiral aperiodic monotile, evolved from ‘equilateral polygon’ tiles, consists of curves instead of straight edges, which brings structural variety to the aperiodic monotile structure. The optimization is carried out in three-dimensional discontinuous design space with the curvature of the chiral aperiodic tile, the volume fraction of each phase, and the selection of materials, considering strength, work of fracture, and failure strain as objective functions. MBO framework is adopted for efficient exploration of optimal designs. Pareto curves are obtained from each optimization of strength-work of fracture and strength-failure strain, and the optimal designs on the Pareto front, which are selected based on strength, work of fracture, failure strain, and balanced manner, are sampled for experimental validation. The optimized designs obtained from the Pareto front show better mechanical properties compared to the benchmark group (which includes square-tiled and hexagon-tiled composite), highlighting the validity of the proposed optimization framework for chiral aperiodic monotile-based composites. Interestingly, the optimized chiral composites prefer to have high curvature (high amplitude of curves), which enables a complex crack path including propagation along the boundary and penetration to cores demonstrating a better balance of mechanical properties than the benchmark designs. We conclude that incorporating a chiral aperiodic monotile pattern into composite structures not only leverages the structural benefits of aperiodicity and the design simplicity which are key advantages of conventional aperiodic monotile structures with straight edges, but also further enhances and fine-tunes their mechanical performance. This research underscores the potential of this new composite family based on chiral aperiodic monotiles, paving the way for developing high-performance structural materials. Additionally, our composite design framework can be adapted for various design objectives with different material compositions, enabling the customization of composite structures that achieve a superior balance of functional performance beyond what the individual constituent materials can offer.

4. Experimental section

Generation of chiral aperiodic monotile composite geometry: The geometric generation process of the chiral aperiodic monotile composite structures is achieved through the following steps. Initially, a ‘hat’ aperiodic monotile is generated using a hexagonal array. This

monotile is then transformed into an ‘equilateral polygon’ tile by adjusting the lengths of its edges, setting the aperiodic shape parameter to 0.5, which makes the area of each tile 28.87 mm². Subsequently, points are calculated at specific distances from the midpoints of each pair of vertices, with these points alternating inside and outside the tile, as shown in Fig. 1a. The spline function is then used to create the curves of chiral aperiodic monotile. Finally, the reinforced tile and its boundary are generated by applying the offset function to each chiral aperiodic monotile. Considering a core volume fraction range of 70 % to 90 % results in the boundary thickness from 0.69 mm to 0.22 mm. More details on the generation of chiral aperiodic monotile structures are provided in Section 5 of the Supporting Information.

Crack phase-field simulation: A key benefit of the crack phase-field model, compared to other fracture modeling techniques (such as cohesive elements), is that it can naturally capture a range of composite failure behaviors like crack initiation, branching, and merging without requiring a predefined crack path. We use the User subroutine function in ABAQUS CAE, a commercial finite element method (FEM) solver, to implement the crack phase-field algorithm. The algorithm used in this study is based on a hybrid formulation [45], which is shown to be adequate for modeling curvilinear crack growth in composite materials, and the implementation of this involves User Element (UEL), User Material (UMAT), and User-defined field (USDFLD) functions in the ABAQUS User subroutine. In the crack phase-field algorithm, the ‘phase’ is a scalar variable between 0 and 1 that represents the damage state of each element. Based on the principle of potential energy balance in a solid body, first introduced by Griffith, the phase field over the entire composite is updated after each deformation step based on the state of the mechanical stress field [46]. The elastic modulus and the stored elastic energy of the elements with a high phase value are degraded irreversibly so that the damaged elements gradually lose their load-bearing capacity. A detailed description of the implementation of the crack phase-field model in the ABAQUS User subroutine and the hybrid formulation is presented in Section 6 of the Supporting information. A comprehensive validation of the implemented crack phase-field model is provided in reference [45].

To minimize the disparity between the simulation and experimental results, experiments are conducted to measure the material properties of the eight types of digital photopolymer materials used in this study, including one hard reinforcement material (VeroClear) and seven soft matrix material candidates (mixture of TangoBlackPlus and VeroClear). For the crack phase field simulation, Young’s modulus (E), Poisson’s ratio (ν), and critical energy release rate (g_c) are required as the material properties. Single-phase test specimens with different digital photopolymer materials are printed and tested under tensile loading, and then the material properties (E , ν , and g_c) are fitted by aligning the stress–strain curves of the simulation to experimental results. Detailed information on material property fitting results and the phase-field simulation condition are presented in Section 1 and Section 6 of the Supporting Information.

Multi-objective Bayesian optimization: To conduct the computations related to the GPR, a Python-based open-source Gaussian process library ‘GPy’ developed by the Sheffield machine learning group is used [47]. Detailed information about the GPR model and our strategy to train the model are provided in Section 7 of the Supporting Information. To effectively handle our design space, which encompasses three ‘non-continuous’ design variables, we customize the GPy library by implementing a special GPR model recently developed by Garrido-Merchan et al. [43]. The GPR model allows for the probabilistic prediction of the objective function, and the acquisition function is computed using the trained GPR to determine the next query point. There are various types of acquisition functions that suggest new input designs in distinct ways, balancing the goal of reaching the optimal objective function value (exploitation) with enhancing the predictive capability of the Gaussian Process Regression (GPR) model (exploration). Here, EHVI is chosen as the acquisition function which is

commonly adopted for MBO to consider both exploration and exploitation in a balanced manner, and we referred to the work by Yang et al. [44] for implementation guidelines.

Uniaxial tensile test: Uniaxial tensile tests (Mode I fracture) are conducted on specimens to fit the material properties of the digital photopolymer materials and specimens for validation purposes. Stratasys Objet350 polyjet printer is used to print the specimens which has a resolution of 600 dpi on the X and Y axes and 1600 dpi on the Z axis. To reduce variability among printed specimens caused by humidity differences during printing, all specimens are printed on the same day. The specimens have dimensions of 50 mm by 125 mm by 3 mm with a notch of 20 % length of the specimen width (10 mm) (See Fig. S10 in Section 8 of the Supporting Information). The top and bottom 25 mm of the specimen are designated as the grip regions. To reduce variation among specimens caused by temperature differences, all samples are stored in a refrigerator at 5 °C for 24 h prior to testing. Mechanical vise action grips are utilized to secure the specimens, clamping only the designated gripping area made of the VeroClear material. The tests are conducted at a controlled tensile displacement rate of 5 mm/min in displacement-control mode. The test terminates when the force is dropped to nearly zero, and the crack is fully propagated through the transverse direction of the specimen. For the notched specimen configuration, we define stress as the external tensile load divided by the cross-sectional area at the notched section (40 mm × 3 mm) and strain as the crosshead displacement divided by the gauge length (75 mm).

CRediT authorship contribution statement

Jiyoung Jung: Writing – original draft, Methodology, Investigation, Formal analysis. **Kundo Park:** Writing – original draft, Methodology, Investigation, Formal analysis. **Grace X. Gu:** Methodology, Investigation, Writing – review & editing, Conceptualization.

Declaration of competing interest

The authors declare that they have no known competing financial interests or personal relationships that could have appeared to influence the work reported in this paper.

Acknowledgments

This research was supported by the Office of Naval Research (Fund Number: N000142112604), Army Research Office (Fund Number: W911NF2420036), Barbara and Gerson Bakar Foundation, and National Science Foundation ACCESS Supercomputing Resources (Fund Number: ACI1548562).

Appendix A. Supplementary data

Supplementary data to this article can be found online at <https://doi.org/10.1016/j.compstruct.2025.119131>.

Data availability

The data that support the findings of this study are available within the article and its [supplementary material](#).

References

- [1] Kim Y, Kim Y, Libonati F, Ryu S. Designing tough isotropic structural composite using computation, 3D printing and testing. *Compos B Eng* 2019;167:736–45.
- [2] Studart AR. Towards high-performance bioinspired composites. *Adv Mater* 2012; 24:5024–44.
- [3] Kuszczak I, Azam F, Bessa M, Tan P, Bosi F. Bayesian optimisation of hexagonal honeycomb metamaterial. *Extreme Mech Lett* 2023;64:102078.
- [4] Gu GX, Takaffoli M, Buehler MJ. Hierarchically enhanced impact resistance of bioinspired composites. *Adv Mater* 2017;29:1700060.

- [5] Moat RJ, Clarke DJ, Carter F, Rust D, Jowers I. A class of aperiodic honeycombs with tuneable mechanical properties. *Appl Mater Today* 2024;37:102127.
- [6] Ghazlan A, Ngo T, Tan P, Xie YM, Tran P, Donough M. Inspiration from Nature's body armours—A review of biological and bioinspired composites. *Compos B Eng* 2021;205:108513.
- [7] Tsai Y-Y, Chiang Y, Buford JL, Tsai M-L, Chen H-C, Chang S-W. Mechanical and crack propagating behavior of sierpiński carpet composites. *ACS Biomater Sci Eng* 2021.
- [8] Lee S, Lim DD, Pegg E, Gu GX. The origin of high-velocity impact response and damage mechanisms for bioinspired composites. *Cell Rep Phys Sci* 2022;101152.
- [9] Wang L, Zeng X, Yang H, Lv X, Guo F, Shi Y, et al. Investigation and application of fractal theory in cement-based materials: A review. *Fractal and Fractional* 2021;5:247.
- [10] Habibi MK, Tam L-h, Lau D, Lu Y. Viscoelastic damping behavior of structural bamboo material and its microstructural origins. *Mech Mater* 2016;97:184–98.
- [11] Zhao H, Yang Z, Guo L. Nacre-inspired composites with different macroscopic dimensions: strategies for improved mechanical performance and applications. *NPG Asia Mater* 2018;10:1–22.
- [12] Archambault P, Janot C. Thermal conductivity of quasicrystals and associated processes. *MRS Bull* 1997;22:48–53.
- [13] Urban K, Feuerbacher M, Wollgarten M. Mechanical behavior of quasicrystals. *MRS Bull* 1997;22:65–8.
- [14] Rabson D. Toward theories of friction and adhesion on quasicrystals. *Prog Surf Sci* 2012;87:253–71.
- [15] Ma X, Duan Y, Huang L, Lei H, Yang X. Quasiperiodic metamaterials with broadband absorption: Tailoring electromagnetic wave by Penrose tiling. *Compos B Eng* 2022;233:109659.
- [16] Ma X, Duan Y, Huang L, Ma B, Lei H. Multicomponent induced localized coupling in Penrose tiling for electromagnetic wave absorption and multiband compatibility. *J Mater Sci Technol* 2022;130:86–92.
- [17] Smith D, Myers JS, Kaplan CS, Goodman-Strauss C. An aperiodic monotile. *arXiv preprint arXiv:230310798*. 2023.
- [18] Clarke DJ, Carter F, Jowers I, Moat RJ. An isotropic zero Poisson's ratio metamaterial based on the aperiodic 'hat' monotile. *Appl Mater Today* 2023;35:101959.
- [19] Naji MM, Al-Rub RKA. Effective elastic properties of novel aperiodic monotile-based lattice metamaterials. *Mater Des* 2024;113102.
- [20] Yan H, Yu H, Zhu S, Wang Z, Zhang Y, Guo L. Nonlinear properties prediction and inverse design of a porous auxetic metamaterial based on neural networks. *Thin-Walled Struct* 2024;197:111717.
- [21] Wang X, Li X, Li Z, Wang Z, Zhai W. Superior strength, toughness, and damage-tolerance observed in microlattices of aperiodic unit cells. *Small* 2024;2307369.
- [22] Jung J, Chen A, Gu GX. Aperiodicity is all you need: Aperiodic monotiles for high-performance composites. *Mater Today* 2024.
- [23] Smith D, Myers JS, Kaplan CS, Goodman-Strauss C. A chiral aperiodic monotile. *arXiv preprint arXiv:230517743*. 2023.
- [24] Snoek J, Larochelle H, Adams RP. Practical bayesian optimization of machine learning algorithms. *Adv Neural Inf Proces Syst* 2012;25.
- [25] Gardner JR, Kusner MJ, Xu ZE, Weinberger KQ, Cunningham JP. Bayesian optimization with inequality constraints. *ICML2014*. p. 937–45.
- [26] Daulton S, Balandat M, Bakshy E. Differentiable expected hypervolume improvement for parallel multi-objective Bayesian optimization. *Adv Neural Inf Proces Syst* 2020;33:9851–64.
- [27] Wu J-Y, Nguyen VP, Nguyen CT, Sutula D, Sinaie S, Bordas SP. Phase-field modeling of fracture. *Adv Appl Mech* 2020;53:1–183.
- [28] Schneider D, Schoof E, Huang Y, Selzer M, Nestler B. Phase-field modeling of crack propagation in multiphase systems. *Comput Methods Appl Mech Eng* 2016;312:186–95.
- [29] Choo J, Sun Y, Fei F. Size effects on the strength and cracking behavior of flawed rocks under uniaxial compression: from laboratory scale to field scale. *Acta Geotech* 2023;1–18.
- [30] Man S, Yu H, Liu S, Wang J. Crack renucleation in bioinspired discontinuous interfaces under thermo-mechanical loading. *Thin-Walled Struct* 2025;208:112837.
- [31] Lumpe TS, Mueller J, Shea K. Tensile properties of multi-material interfaces in 3D printed parts. *Mater Des* 2019;162:1–9.
- [32] Rahul Kumar P, Jagota A, Bennison S, Saigal S. Cohesive element modeling of viscoelastic fracture: application to peel testing of polymers. *Int J Solids Struct* 2000;37:1873–97.
- [33] Khalil Z, Elghazouli AY, Martinez-Paneda E. A generalised phase field model for fatigue crack growth in elastic-plastic solids with an efficient monolithic solver. *Comput Methods Appl Mech Eng* 2022;388:114286.
- [34] Li P, Li W, Li B, Yang S, Shen Y, Wang Q, et al. A review on phase field models for fracture and fatigue. *Eng Fract Mech* 2023;289:109419.
- [35] Li P, Li W, Tan Y, Fan H, Wang Q. A phase field fracture model for ultra-thin micro-/nano-films with surface effects. *Int J Eng Sci* 2024;195:104004.
- [36] Park K, Scaccabarozzi D, Sbaruffatti C, Jimenez-Suarez A, Urena A, Ryu S, et al. Coupled health monitoring system for CNT-doped self-sensing composites. *Carbon* 2020;166:193–204.
- [37] Park K, Song C, Park J, Ryu S. Multi-objective Bayesian optimization for the design of nacre-inspired composites: optimizing and understanding biomimetics through AI. *Mater Horiz* 2023;10:4329–43.
- [38] Wang K, Dowling AW. Bayesian optimization for chemical products and functional materials. *Curr Opin Chem Eng* 2022;36:100728.
- [39] Khatamsaz D, Vela B, Singh P, Johnson DD, Allaire D, Arróyave R. Multi-objective materials bayesian optimization with active learning of design constraints: Design of ductile refractory multi-principal-element alloys. *Acta Mater* 2022;236:118133.
- [40] Yang Z, Park K, Nam J, Cho J, Choi YJ, Kim YI, et al. Multi-objective bayesian optimization for laminate-inspired mechanically reinforced piezoelectric self-powered sensing yarns. *Adv Sci* 2024;11:2402440.
- [41] Deneault JR, Chang J, Myung J, Hooper D, Armstrong A, Pitt M, et al. Toward autonomous additive manufacturing: Bayesian optimization on a 3D printer. *MRS Bull* 2021;46:566–75.
- [42] Motoyama Y, Tamura R, Yoshimi K, Terayama K, Ueno T, Tsuda K. Bayesian optimization package: PHYSBO. *Comput Phys Commun* 2022;278:108405.
- [43] Garrido-Merchán EC, Hernández-Lobato D. Dealing with categorical and integer-valued variables in bayesian optimization with gaussian processes. *Neurocomputing* 2020;380:20–35.
- [44] Yang K, Emmerich M, Deutz A, Bäck T. Efficient computation of expected hypervolume improvement using box decomposition algorithms. *J Glob Optim* 2019;75:3–34.
- [45] Jeong H, Signetti S, Han T-S, Ryu S. Phase field modeling of crack propagation under combined shear and tensile loading with hybrid formulation. *Comput Mater Sci* 2018;155:483–92.
- [46] Molnár G, Gravouil A. 2D and 3D Abaqus implementation of a robust staggered phase-field solution for modeling brittle fracture. *Finite Elem Anal Des* 2017;130:27–38.
- [47] GPY. GPY: A Gaussian process framework in python. <http://github.com/SheffieldML/GPy>. since 2012.